Phytopathology® • 2023 • 113:1439-1446 • https://doi.org/10.1094/PHYTO-01-23-0030-R

Ecology and Epidemiology

Scalable Early Detection of Grapevine Viral Infection with Airborne Imaging Spectroscopy

Fernando E. Romero Galvan,[1,†] Ryan Pavlick,[2] Graham Trolley,[3] Somil Aggarwal,[1] Daniel Sousa,[4] Charles Starr,[5] Elisabeth Forrestel,[6] Stephanie Bolton,[7] Maria del Mar Alsina,[8] Nick Dokoozlian,[8] and Kaitlin M. Gold[1]

[1] Cornell University, Cornell AgriTech, Geneva, NY 14456
[2] Jet Propulsion Laboratory, California Institute of Technology, Pasadena, CA 91109
[3] University of Connecticut, Stamford, CT 06901
[4] San Diego State University, San Diego, CA 92182
[5] Viticultural Services, Lodi, CA 95220
[6] University of California, Davis, CA 95616
[7] Lodi Winegrape Commission, Lodi, CA 95242
[8] E. & J. Gallo, Modesto, CA 95354

Accepted for publication 19 April 2023.

Abstract

The U.S. wine and grape industry loses $3B annually due to viral diseases including grapevine leafroll-associated virus complex 3 (GLRaV-3). Current detection methods are labor-intensive and expensive. GLRaV-3 has a latent period in which the vines are infected but do not display visible symptoms, making it an ideal model to evaluate the scalability of imaging spectroscopy-based disease detection. The NASA Airborne Visible and Infrared Imaging Spectrometer Next Generation was deployed to detect GLRaV-3 in Cabernet Sauvignon grapevines in Lodi, CA in September 2020. Foliage was removed from the vines as part of mechanical harvest soon after image acquisition. In September of both 2020 and 2021, industry collaborators scouted 317 hectares on a vine-by-vine basis for visible viral symptoms and collected a subset for molecular confirmation testing. Symptomatic grapevines identified in 2021 were assumed to have been latently infected at the time of image acquisition. Random forest models were trained on a spectroscopic signal of noninfected and GLRaV-3 infected grapevines balanced with synthetic minority oversampling of noninfected and GLRaV-3 infected grapevines. The models were able to differentiate between noninfected and GLRaV-3 infected vines both pre- and postsymptomatically at 1 to 5 m resolution. The best-performing models had 87% accuracy distinguishing between noninfected and asymptomatic vines, and 85% accuracy distinguishing between noninfected and asymptomatic + symptomatic vines. The importance of nonvisible wavelengths suggests that this capacity is driven by disease-induced changes to plant physiology. The results lay a foundation for using the forthcoming hyperspectral satellite Surface Biology and Geology for regional disease monitoring in grapevine and other crop species.

Keywords: AVIRIS next generation, early detection, grapevine leafroll-associated virus 3, imaging spectroscopy, scalable

Plant–microbe interactions impact a variety of plant traits that can be sensed remotely, ranging from changes in tissue color to canopy architecture (Agrios 2009). Broadband methods relying primarily on visible (VIS) and near-infrared (NIR) spectral indices, such as the normalized difference vegetation index (NDVI), were proven capable of sensing late-stage plant disease in the 1980s (Jackson 1986; Nagarajan 1984). However, the advent of more widely available narrowband data streams spanning the VIS–shortwave infrared (SWIR) range has revolutionized the study of plant disease sensing. Plant pathogens damage, impair, and/or alter foliar function, thus changing the chemical composition of foliage via the production of either systemic effectors or secondary metabolites. The changes can be sensed with in situ and imaging spectroscopy often referred to by plant pathologists as "hyperspectral imaging" (Gold et al. 2020a). SWIR wavelengths have proven valuable for plant–pathogen interaction sensing due to their sensitivity to a range of foliar properties (Curran 1989), including nutrient content (Singh et al. 2015), water (Gao 1996), photosynthetic capacity (Oren et al. 1986), physiology (Serbin et al. 2019), phenolics and secondary metabolites (Couture et al. 2016), that are all impacted during infection and early-stage disease. Recent work has established that airborne imaging spectroscopy is capable of presymptomatic disease detection in multiple pathosystems, including olive quick decline syndrome OQDS caused by *Xylella fastidiosa* (Zarco-Tejada et al. 2018, 2021), infection of Holm oak by *Phytophthora* spp. (Hornero et al. 2021), and infection of oak by *Bretziella fagacearum* (Sapes et al. 2022). These collective works demonstrate that airborne sensing not only can provide reliable asymptomatic disease detection, but in some instances, it outperformed human scouting by detecting minimally symptomatic trees missed by the ground-truthing team (Zarco-Tejada et al. 2021).

Disease detection via imaging spectroscopy is often facilitated by machine learning, which helps to make sense of the underlying

---

[†] Corresponding author: F. E. R. Galvan; fer36@cornell.edu

Funding: Support was provided, in part, by the Jet Propulsion Laboratory, California Institute of Technology, under a contract with the National Aeronautics and Space Administration (NASA; 80NM00018D0004), the NASA FINESST Grant (80NSSC21K1605), the NASA Jet Propulsion Laboratory Strategic University Research Partnership Fund, and the NASA Biodiversity and Ecological Forecasting Program. F. E. R. Galvan received funding from the National Science Foundation NRT Digital Plant Sciences Grant awarded to Cornell University (grant 1922551). D. Sousa received funding from the U.S. Department of Agriculture-National Institute of Food and Agriculture Sustainable Agroecosystems Program (grant 2022-67019-36397), the NASA Land-Cover/Land Use Change Program (grant 21-LCLUC21 2-0025), the NASA Remote Sensing of Water Quality Program (grant 80NSSC22K0907), and the National Science Foundation Signals in the Soil Program (award 2226649).

e-Xtra: Supplementary material is available online.

The author(s) declare no conflict of interest.

relationships within and among the hundreds of (highly correlated) spectral bands that the approach offers (Maxwell et al. 2018; Meza Ramirez et al. 2021). Machine learning methods such as random forest (RF) and partial least squares have been used widely in airborne plant–microbe interaction sensing, including mycorrhizal association mapping (Sousa et al. 2021), oak wilt detection (Sapes et al. 2022), and olive quick decline syndrome mapping (Calderón et al. 2013; Zarco-Tejada et al. 2018), as well as in the broader adjacent domains of foliar functional ecology (Martin et al. 2018; Schneider et al. 2017).

While the above-mentioned studies have shown that imaging spectroscopy can be useful in understanding, detecting, and mapping plant–fungal and bacterial–fungal interactions, viral–plant interactions remain to be explored. Viral diseases, including that caused by grapevine leafroll virus complex 3 (GLRaV-3), cause U.S. $3 billion in losses to the U.S. wine and grape industry annually (Naidu et al. 2014). GLRaV-3 is primarily vectored by mealybugs (Pseudococcidae spp.) but can also be transmitted by other phloem-feeding insects (Charles et al. 2009; Pietersen et al. 2013). In addition to significantly reducing vine lifespan, GLRaV-3 infection causes the grapevine to misappropriate resources, which results in uneven cluster ripening, changes in grape berry chemistry, and reduced wine quality (Naidu et al. 2014; Song et al. 2021). Existing strategies to detect GLRaV-3 in the field are based on visual scouting by trained experts (Bolton 2020). However, managing GLRaV-3 is particularly challenging because only red grape varieties, such as Cabernet Sauvignon (unlike Sauvignon Blanc), display foliar symptoms, which are necessary for scouts to detect the disease (Naidu et al. 2015). Compounding this is the fact that GLRaV-3 has a long (approximately 12-month) latent phase during which the host is infectious but foliar symptoms are not yet apparent (Blaisdell et al. 2016; Naidu et al. 2014; Olmos et al. 2016). This means that both latently infected red grape varieties and infected white grape varieties serve as inoculum sources for nearby fields without grower recourse other than expensive molecular testing. Commercial lab-based serological testing capable of identifying latent infections costs between U.S. $40 and 300 per vine, depending on how many viruses are tested for and whether composite sampling is utilized. Even a small-scale vineyard will have at least 1,000 vines, with larger vineyards having up to 30,000 vines, making both regular and asymptomatic testing prohibitively costly to scale.

Consequently, plant pathologists and grape growers have begun to look for a detection approach that is both temporally and spatially scalable, accurate, and cost-effective. Remote sensing's capacity for scalable, passive disease monitoring makes it of great interest to plant pathology and the broader agricultural science communities. Proof-of-concept work has established that contact and proximal spectroscopy can detect GLRaV-3 infection at an early stage (Bendel et al. 2020; Gao et al. 2020; Naidu et al. 2009; Sinha et al. 2019). Furthermore, MacDonald et al. (2016) found that spectroscopic imagery, the data product of the imaging spectroscopy approach, can be used to develop models to differentiate between GLRaV-3 symptomatic and noninfected grapevine. However, it has yet to be determined whether the detection capability scales to suborbital (e.g., airborne) deployment.

NASA's Airborne Visible/Infrared Imaging Spectrometer Next Generation (AVIRIS-NG) is an airborne instrument operated from the Jet Propulsion Laboratory in Pasadena, CA with extensive historic acquisitions in California, including over ∼364,000 ha of vineyards. The AVIRIS mission family, which includes Classic (C), Next Generation (NG), and the forthcoming AVIRIS-3, will continue to collect wide-swath, high-spectral-resolution (<10 nm), and highly uniform spectroscopic imagery (400 to 2400 nm) over diverse California biomes, including agricultural production areas. Therefore, it is a perfect opportunity to generalize, optimize, and continuously validate plant disease detection models. The goal of this project was to evaluate the scalability of airborne-imaging-spectroscopy-based detection of symptomatic and asymptomatic grape viral disease with AVIRIS-NG using flight lines deployed over vineyards known to have vines infected with GLRaV-3. Specifically, we sought to determine the following. (i) How accurately does airborne imaging spectroscopy differentiate between noninfected and GLRaV-3 infected vines? (ii) Can detection be improved with various dimensionality reduction techniques? (iii) What is the optimal resolution for GLRaV-3 detection within the range of 1 to 5 m?

Materials and Methods

Ground validation

Industry collaborators coordinated a team of trained field technicians to visually inspect ("scout") 109 ha of the red grape varieties Aglianico (3 ha), Cabernet Sauvignon (83 ha), and Petite Sirah (23 ha) for visible foliar symptoms of GLRaV-3 according to industry best practices (Bolton 2020). Further information on how scouting teams are instructed can be found in Bolton (2020). In brief, scouts were trained to recognize foliar symptoms of GLRaV-3 (Fig. 1). The symptoms include foliar reddening with green veins, mild chlorosis, and curling of the leaf edges. Vine spacing was 1.5 m between rows and 1 m in rows. Scouting and geotagging of visibly diseased vines (Fig. 1) were conducted in September of 2020 and 2021, during harvest, when symptoms are most apparent. In total, 1,427 and 2,398 GLRaV-3-infected vines were identified by the ground-scouting teams in 2020 and 2021, respectively. All grape clusters, green foliage, and canes were removed from the grapevines during mechanical harvest approximately 1 week after final airborne data acquisition in 2020. Cane tissue samples from 100 vines in 2020 and 10 vines in 2021, variably identified as diseased/nondiseased,

Fig. 1. Symptoms of grapevine leafroll-associated virus complex 3 (GLRaV-3) infection in a grapevine (Cabernet Sauvignon). Characteristic reddening of the foliage can be seen in the upper leaves of the grapevine. Leaves displaying no obvious foliar symptoms can also be seen in the image.

were sent to Agri-Analysis Laboratories (Davis, CA) for GLRaV-3 virus diagnostic testing to validate scouting accuracy. All samples sent for testing that had been identified as GLRaV-3-infected by the scouts returned positive for infection. No samples that were identified as noninfected by the scouts tested positive, giving us high confidence in the scouting teams' accuracy. After mechanical harvest in 2020 and prior to 2021 bud break, the industry collaborators removed diseased vines from the vineyards to prevent them from serving as an inoculum reservoir for uninfected grapevines. Therefore, vines identified as diseased in 2020 were not present in the vineyards in 2021.

Imagery acquisition

In September 2020, spectroscopic imagery over vineyards in Lodi was acquired with NASA-JPL's AVIRIS-NG instrument on board a King Air B-200 aircraft from an altitude of ~1,000 m above ground level. In total, this campaign, the "AVIRIS Wine Tour," collected imagery over 15,095 ha of California vineyards spanning Napa Valley, Sonoma Valley, Lodi, and Paso Robles, at peak grapevine foliage. Each AVIRIS-NG flight line (acquisition) was collected at <1 m spatial resolution. The AVIRIS-NG platform samples the electromagnetic (EM) spectrum at 5-nm intervals within the 380- to 2,510-nm spectral range, resulting in 425 spectral channels (Chapman et al. 2019; Thompson et al. 2018). Acquisitions were collected between 1300 and 1500 Pacific (local) time. An 83-ha subset of the imagery collected from Cabernet Sauvignon grapevines was used for this study (Supplementary Fig. S2). The specific acquisition IDs are ang20200918t210249, ang20200918t205737, ang20200918t212656, ang20200918t213801, and ang20200918 t213229. All AVIRIS-NG imaging used in this study is reflectance data, is publicly available, and can be downloaded from the AVIRIS-NG data portal: https://aviris.jpl.nasa.gov/dataportal/.

Data processing and cleaning

Generic spectra for soil, vegetation, and shadow were used as endmembers for spectral unmixing. The soil and vegetation spectra were pulled from the United States Geological Survey Spectroscopy Laboratory's spectral library (Kokaly et al. 2017). The U.S. Geological Survey spectral measurements were selected because they matched the spectral range of the AVIRIS-NG imagery in terms of spectral resolution. Additionally, the Lodi team provided ground-spectral measurements of grass pastures, soil, pavement, and vines for calibration and validation purposes (Supplementary Fig. S4). The entirety of the pipeline was written in Python 3.9 (Fig. 2). All scripts are available from the GoldLab-Github repository (https://github.coecis.cornell.edu/GoldLab-GrapeSPEC). Anaconda was used for Python package management; likewise, Anaconda virtual environments have been uploaded to the GoldLab-GitHub.

A bidirectional reflectance distribution function and a topographic correction (Queally et al. 2022) were applied to all reflectance files of the entire AVIRIS-NG flight line. Bidirectional reflectance distribution function and topographic correction code were pulled from the HyTools package (Chlus et al. 2023), an open-source spectroscopy processing Python library. Some of the AVIRIS-NG imagery required further spatial georeferencing to be better aligned with the disease incidence coordinates collected by the scouting team. Imagery collected by the National Agriculture Imagery Program (NAIP; USDA; https://naip-usdaonline.hub.arcgis.com/) within 1 week of the AVIRIS-NG imagery acquisition was used as a reference to improve georeferencing and co-registration. Each NAIP image was clipped according to the area of overlap with the AVIRIS-NG image. Specifically, the NAIP red band was extracted and compared with the AVIRIS-NG band at 600 nm. Ground control points were generated by passing the described target and reference imagery to the open-source Python library Automated and Robust Open-Source Image Co-registration Software (AROSICS) (Scheffler et al. 2017). For higher specificity and co-registration of images, AROSICS was parameterized according to the code-base author's default parameters. The resulting ground control points were used to co-register the AVIRIS-NG imagery onto the NAIP imagery. Last, following standard practice, noisy bands (due to water absorption and other atmospheric effects) present in the data were excluded following a visual analysis; these are the wavelengths between 380 and 400 nm, 1,310 and 1,470 nm, 1,750 and 2,000 nm, and 2,400 and 2,600 nm. The excluded wavelengths are illustrated as gaps (Fig. 3; Supplementary Figs. S1, S4, and S5).

Vineyard boundaries shared by industry collaborators were used to mask the AVIRIS-NG imagery. The open-source Python library Rasterio's mask package was used for clipping the imagery (Gillies et al. 2013). The opensource HyTools library included a command line interface (CLI) Python spatial resampling script that was used to resample the clipped co-registered imagery from the native 1- to 3-m and 5-m resolution. The spatial resampling script used applies

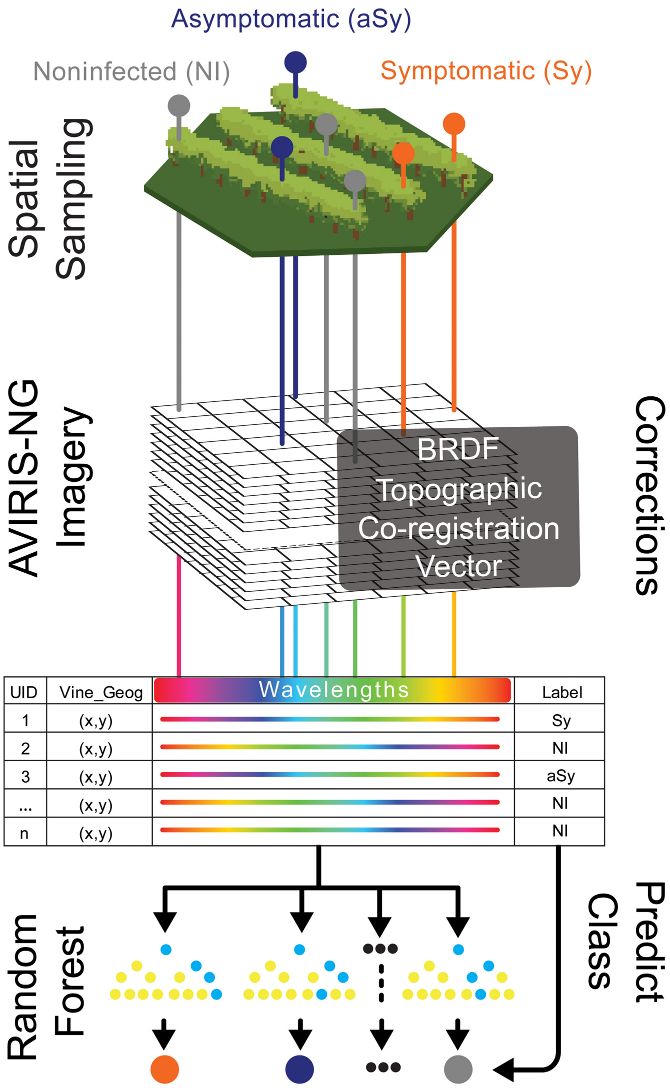

Fig. 2. An illustrative summary of the methodology used in the study. First, the grapevine leafroll-associated virus complex 3 (GLRaV-3) incidence coordinates are used to spatially sample the Airborne Visible and Infrared Imaging Spectrometer Next Generation (AVIRIS-NG) spectroscopic imagery. Second, the 2020 GLRaV-3 incidence is used to generate the symptomatic (Sy) dataset while the 2021 GLRaV-3 incidence is used to generate the asymptomatic (aSy) dataset. Third, a list of corrections applied to the AVIRIS-NG spectroscopic imagery is indicated, as well as how the data are converted into a tabular dataframe. Fourth, the dataframe is used to train a random forest model to predict the class of the grapevine using the wavelengths included in the spectroscopic image.

the nearest-neighbor algorithm with no blurring effects to resample the image.

The spectral mixture residuals (SMRs) were computed using the open-source code of Sousa et al. (2022). Endmembers for shadow, soil, and generic vegetation were used to spectrally unmix the AVIRIS imagery (Supplementary Fig. S3). The SMR simultaneously estimates two related parameters for each pixel in the image: (i) fractional area of each input endmember and (ii) mixture residual spectra quantifying wavelength-explicit misfit. Soil masks for each vineyard were generated by calculating a percentage of vegetation and soil endmember weights calculated by the SMR script. The equation used was $Vw/(Vw + Sw)$, where Vw is the vegetation endmember fractal weight and Sw is the soil endmember fractal weight. The resulting raster was used to create a binary mask: all pixels with a value ≥ 0.50 were assigned a one, and all remaining pixels were assigned a zero. A percentage of 0.5 was found to be optimal both to preserve disease incidence and to remove most soil pixels. This binary mask was applied to all clipped imagery, retaining only pixels sampling a minimal area that was not covered with grapevine canopy.

Data analysis

The dataset consists of three labels: noninfected (NI), symptomatic (Sy), and asymptomatic (aSy). These acronyms are used when referring to dataset labels. Vines that were not identified as visibly diseased by scouting teams in 2020 or 2021 are labeled as noninfected (NI). Vines identified as visibly diseased in 2020 (the data acquisition year) are labeled as symptomatic (Sy). These vines were removed from the vineyards during winter dormancy before the 2021 growing season (bud break). Vines identified as visibly diseased in 2021 are labeled as asymptomatic (aSy). These vines were NOT visibly diseased in 2020, implying they were latently infected during the 2020 AVIRIS-NG flights. Green tissue is required for the insect vector to feed upon and transmit GLRaV-3. Red grape variety vines infected with GLRaV-3 can remain asymptomatic for up to a year if visible symptoms do not manifest before winter dormancy (Blaisdell et al. 2016; Charles et al. 2006; Olmos et al. 2016). Winter dormancy begins when all green foliage is shed or forcibly removed during mechanical harvest and the season's green cane tissue hardens and forms bark. It is unlikely that grapevines labeled as aSy in our dataset became infected after the 2020 AVIRIS-NG data acquisition and before the 2021 bud break. However, we must note that molecular testing was not conducted to diagnose conclusively whether vines we label as aSy were truly asymptomatic during the 2020 data acquisition. Molecular testing was not possible given the study's scope and the expense of sample testing (approximately \$40 to \$50 per vine). Our assumption that vines identified as visibly diseased in 2021 were latently infected during the 2020 data acquisition is well supported by the current understanding of GLRaV-3 disease biology (Almeida et al. 2013; Blaisdell et al. 2016; Maree et al. 2013; Naidu et al. 2014) and the fact that all green foliage was removed from the vineyard during mechanical harvest shortly after the AVIRIS-NG image data acquisition flight.

To generate "noninfected" vine locations, clipped, co-registered, and soil-masked imagery was vectorized by extracting the centroid for all pixels within the image. GLRaV-3 infected vines are spatially clustered (Arnold et al. 2017; Cabaleiro and Segura 2006; Habili and Nutter 1997), so centroids within a 5-m buffer of the known diseased coordinates were excluded to avoid accidentally labeling vines as "noninfected" that may not truly be nondiseased. In total 621,000, 70,000, and 27,000 noninfected vine pixels were counted using this procedure for the 1-, 3-, and 5-m spatial resamplings, respectively. The pixel count for aSy was 2,258, 2,458, and 2,192 for the 1-, 3-, and 5-m resamplings, and the pixel count for Sy was 1,027, 1,139, and 1,031 for 1, 3, and 5 m, respectively. The pixel count for the class where aSy and Sy were treated together was 3,285, 3,597, and 3,223 for 1-, 3-, and 5-m resamplings, respectively.

Spectral transformations of various types were considered and tested to reduce noise, dimensionality, and correlation between wavelengths in the AVIRIS-NG imagery. First, the SMR output was used as the feature for the RF to train on. Second, the Savitzky–Golay (SG) filter from the signal module in the Scipy python package was applied to the data (Virtanen et al. 2020). SG is a commonly used filtering method for random noise reduction in spectroscopic signal processing (Tsai and Philpot 1998). The SG smoothing window was limited to five wavelengths and a polynomial order of three. Third, SKLearn's PCA library was used to perform a principal components analysis (PCA) on the spectral feature space to reduce the dimensionality of the feature space from 425 to 10 principal components (PCs). Fourth and last, a combination of all techniques above was used as the feature set for the later training of the RF model. All noise-reduction and dimensionality-reduction techniques excluded noisy wavelengths due to atmospheric water content, as is standard for airborne imaging spectroscopy.

Vine coordinates labeled by their GLRaV-3 infection status (NI, Sy, and aSy) were loaded onto a Geopandas data frame. All coordinates were stored and reprojected to the AVIRIS-NG acquisition's coordinate system WGS 84/UTM zone 10N; EPSG: 32610. Each

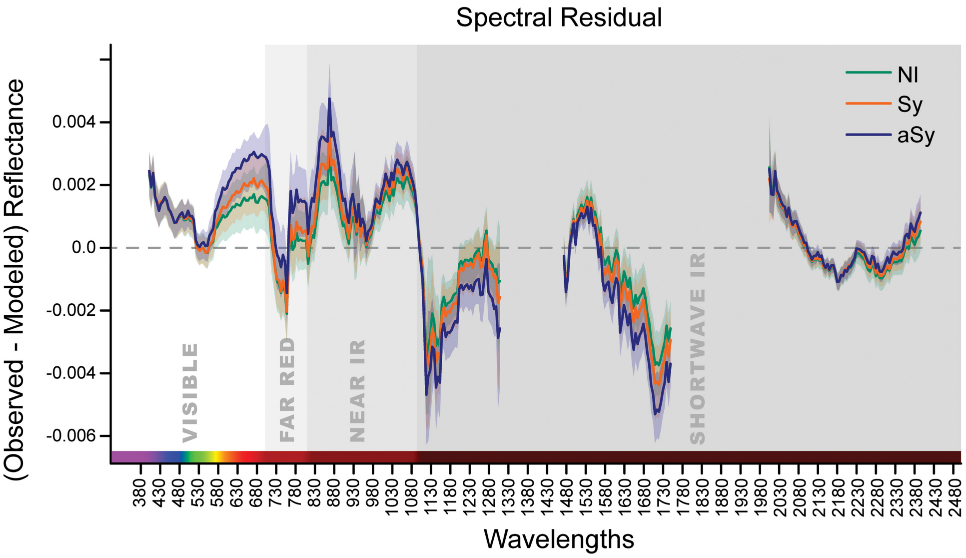

Fig. 3. Spectrally unmixed residuals by grapevine leafroll-associated virus complex 3 infection status showing the symptomatic (Sy), asymptomatic (aSy), and noninfected (NI) classes. The various shading in the background of the electromagnetic spectrum represents the visible, far red, near infrared (near IR), and shortwave infrared (shortwave IR) wavelength regions of the spectrum.

coordinate was used to sample the AVIRIS-NG imagery spatially, resulting in a data frame that held the coordinate, label, unique field name, and relevant spectral data. NI vines far outnumber Sy + aSy vines combined. Noninfected to diseased ratios were approximately 3,109:18, 700:33, and 175:9 for 1-, 3-, and 5-m resamplings, respectively, which presented a challenge in choosing a balancing strategy. In order to generate a representative population of NI vines to train on, we employed both under- and oversampling. To undersample, a PCA was performed on all NI vine spectra. Three PCs explained 95% of the variance of the NI-vine spectra. The resulting PC space was clustered using SKLearn's K-means clustering library, and three K-means were found to be optimal to cluster the data using the "elbow method," where distortion is plotted against the number of clusters to establish a cutoff. In this case, three-clusters were found to be optimal. Next, an equal number of points were randomly selected from the resulting three-dimensional cluster feature space. In total, 3,200 NI spectral rows were sampled from 1-m resampling, 3,500 from 3-m resampling, and 3,200 from the 5-m resampling, respectively.

Next, Imbalanced Learn's (Lemaître et al. 2017) Synthetic Minority Oversampling Technique (SMOTE) was used for oversampling. First, the diseased incidence points were oversampled using SMOTE to increase their count by 10, 25, 50, 75, 100, 200, and 300%. It was found that an increase of 50% oversampling of the minority class was optimal. Second, SKLearn's RF Python package was used for RF model training (Pedregosa et al. 2011). The now balanced datasets were used to train 10 RF models, and performance was averaged across the models for the validation set. The training/validation data was split 70/30 and 10 *k*-folds were performed on each training. All steps were repeated for all transformations done to the spectra and across the 3- and 5-m resolution data. Partial least squares discriminant analysis (PLS-DA) was briefly investigated as an alternative approach to RF. A model discriminating between NI and (aSY + Sy) was trained on both raw reflectance values and 10 PCA; however, little to no difference was found between PLS-DA and RF accuracy. The PLS-DA model performed best at 1 and 5 m with similar accuracy and kappa scores peaking at 79% and 0.57, respectively (data not shown). PLS approaches can be prone to overfitting and take significantly longer to compute than RF, so this avenue of analysis was not investigated further.

Results

All models developed during the study followed a 70/30 training and validation scheme. All accuracy and respective kappa scores are derived from the 30% validation data withheld during training and are reported in Supplementary Table S1. Each metric presented is the result of the average performance of 10 models trained on different splits of training and validation datasets. To generate a baseline accuracy, a RF model was trained on the reflectance values to classify the row according to its GLRaV-3 infection status label (NI, aSy, and Sy). This model at best differentiated between NI and aSy labels at 1-m resolution with 75% accuracy and a 0.50 kappa score. Next, a RF model was trained on reflectance values with SG smoothing applied; at best this model differentiated between NI and aSy at 3-m resolution (80% accuracy, 0.58 kappa score). Next, 10 PCs were generated from the SG filtered spectra and used to train the RF SG PCA model; this model performed best at differentiating between NI and aSy labels at 3 m with an 83% accuracy and 0.66 kappa score. The original reflectance data were then used to calculate the SMRs; this dataset was used to train the RF model RF MR, which performed best at differentiating between NI and aSy labels at 3-m and 5-m resolution with 77% accuracy for both models, and kappa scores of 0.51 at 3 m and 0.54 at 5 m, respectively. The MR dataset was used to calculate a new set of 10 PCs to be used as features to train the RF MR PCA model; this model performed best at differentiating between NI and aSy labels at 1 and 5 m, with accuracy/kappa scores of 79%/0.58 and 77%/0.54, respectively.

Overall, the two best-performing models were for discrimination between the NI versus aSy and NI versus aSy + Sy labels. In both cases, the best-performing models were those that were trained on 3-m resolution spectroscopic imagery with SG applied and then lowered in dimensionality to 10 PCs. In both cases, the model training data followed a balancing strategy that first undersampled the majority class and oversampled the minority class via SMOTE (Supplementary Table S1). The two models had 87% accuracy (0.73 kappa) and 85% accuracy (0.71 kappa), respectively, in discriminating between NI and (aSy + Sy) vines. In all cases, the diseased label, regardless of aSy or Sy status, was differentiable from the NI vine spectra (Fig. 4).

Generally, model accuracy did not vary significantly across spatial scales ranging from the native resolution (1 m) to the resampled 3- and 5-m resolutions (Supplementary Table S1). The RF model performed best at 3-m spatial resolution, with a decrease in accuracy at 5 and 1 m. The 3-m SG-PCA-SMOTE model discriminating between NI and aSy + Sy with the appropriate data corrections and transformations applied was found to be the most accurate model (87% accuracy and a 0.73 kappa score). The model was used to classify any pixel with a >50% probability as infected (Fig. 5). While the model was accurate overall, it overclassifies areas as diseased (aSy or Sy) compared with the observed diseased extent. Misclassification swathes tend to cluster near the edges of the vineyard boundary.

Illustrating the MR (Fig. 3) provides insight into why the GLRaV-3 Sy, aSy, and NI classes are differentiable by the ML models. The figure shows that most of the differences are in the SWIR (1,130 to 1,330 nm and 1,530 to 1,730 nm), NIR (820 to 880 nm), and VIS (580 to 680 nm) regions. Although the differences are subtle and difficult to find by inspecting the spectral signal (Supplementary Fig. S1), visualizing the MR allows the differences between the vine classes to be more readily observed.

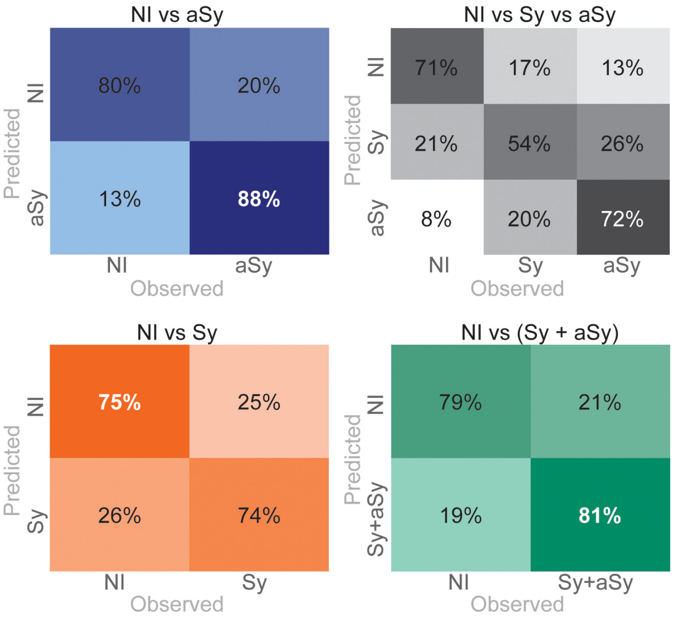

Fig. 4. The confusion matrices based on validation datasets for the random forest (RF) model trained on 3-m-resolution imagery with Savitzky–Golay (SG) filtering, principal components analysis (PCA), and undersampling and oversampling class balancing strategies (labeled RF SG PCA SMOTE in Supplementary Table S1). The model predictions follow the *y*-axis, while the observed label follows the *x*-axis. Here, we show the true and false positive as well as the true and false negative rates of the validation dataset (the dataset excluded from training) for each labeling strategy: noninfected (NI) versus asymptomatic (aSy), NI versus symptomatic (Sy), NI versus Sy versus aSy, and NI versus (Sy + aSy) treating both labels as one class.

Discussion

Surprisingly, the aSy vine native spectral signature and the signature in the spectral residual feature space were the most notably different from the Sy and NI classes. This suggests that asymptomatic GLRaV-3 vines have a unique spectral signature that differentiates them from *both* noninfected and symptomatic grapevines. This finding that all three classes differ spectrally supports the assumption that the aSy-labeled vines were indeed experiencing latent infection at the time of data acquisition. In classifying between all three classes, most misclassifications are between Sy and aSy vines, indicating that these two groups share enough spectral similarity for the models to confuse them. The spectral similarity may be explained by the GLRaV-3-infection, which is known to affect vine biology prior to symptom appearance (Gao et al. 2020; Naidu et al. 2009; Sinha et al. 2019). We find that SWIR wavelengths are the most important for accurate differentiation of the classes. This spectral region is known to be strongly associated with plant chemistry and physiology (Curran 1989), implying that the spectral differences we see likely originate in differences between non-, pre-, and post-symptomatic vine physiology. Thus, we find that "full-spectrum" (aka VSWIR) imagery is necessary for accurate asymptomatic disease detection. We see this reflected again in the performance of the models trained on the aSy dataset only and on that combined with the Sy dataset. The result is surprising, considering that visually, an asymptomatic vine cannot be differentiated from a noninfected vine. However, the results in this study suggest that asymptomatic vines are in fact the most spectrally differentiable not only from noninfected, but also from symptomatic vines.

The resulting pixel size of airborne spectroscopic imagery is dependent on the height at which the aircraft is flown. Therefore, the exact AVIRIS-NG pixel size achieved can be unpredictable, though the spatial resolution will commonly be between 1 and 5 m. Our models generally performed best at 3-m spatial resolution. Likely, the loss of accuracy in going from 3- to 5-m resolution is due to the dilution of the spectral signal that underlies the ability to discriminate between groups. In this study it was anticipated that detection would be most accurate at the native 1-m resolution, but the results show otherwise. This may be because each individual diseased vine, despite the geotag being accurate at <1 m resolution, is sometimes at the edge of multiple pixels, which may conflate the signal. Additionally, at 1-m resolution, there is less dilution of factors that cause noise in the spectra, such as soil patches, grass, and other nonvine reflectance. The results suggest that for the vine spacing in the vineyards used (1 m × 1.5 m), 3-m resampling was the optimal balance point between minimizing noise and not overdiluting the dataset.

Our most accurate model, the 3-m SG-PCA-SMOTE model differentiating between NI and Sy + aSy, is prone to misclassification near vineyard boundaries, which we suspect is due to confounding instances of biotic (disease) and abiotic stress. Vines at the ends of the row are known to experience more stress than buffered inner vines. This includes more exposure to contrasting environmental factors and uneven management practice (e.g., irrigation being less near the row end). Untangling biotic and abiotic stressors is a major challenge to accurate plant–pathogen interaction mapping with imaging spectroscopy. Additionally, vineyards are not sterile environments, and it is likely that an infected vine may have a combination of stressors affecting it, including pest damage. The border regions tend to experience more stress; thus, these vines are most likely to have a baseline stressed profile that our model finds more like a diseased spectral profile at this scale of study. Alternatively, in some cases the confusion may be due to stress caused by an overabundance of water (waterlogging; Zhu et al. 2018). Proximity to water, such as a river's edge (Fig. 5), can increase the likelihood of an unhealthy root system that may become infected by various fungal pathogens, especially for grapevines with typically deep root systems.

One of the greatest challenges in disease detection via imaging spectroscopy is untangling the signal sof abiotic and biotic stressors that may be affecting a vine simultaneously. Typical vineyard abiotic stressors, including water stress or nutrient deficiency, are closely related to thermal data (Calderón et al. 2013; López-López et al. 2016). Abiotic and biotic stresses, even those with a common visual manifestation (e.g., wilt), can be differentiated with airborne sensing because their underlying biological origins are different (Zarco-Tejada et al. 2021). Multimodal sensing complements imaging-spectroscopy-based disease detection by adding biologically relevant data that can be useful for untangling biotic and abiotic stress. In other pathosystems, solar-induced fluorescence has proven useful considering the close relationship between SIF and photosynthetic activity (Sun et al. 2017). However, calculating solar-induced fluorescence requires a narrower-band instrument (0.3 nm) than that on board AVIRIS-NG (5 nm). Adding thermal and solar-induced fluorescence products in combination with spectral unmixing approaches, such as SMR or multiple endmember spectral mixture analysis, could help provide a clearer picture of the biological origins, biotic or abiotic, of crop stress. Despite these challenges, we find that imaging spectroscopy continues to be a rapid and accurate tool for mapping GLRaV-3.

Geography plays an important role in the generalizability of all remote sensing applications. The models developed here consider only central California, where the soil type, grape variety, regional vineyard management practices, and climate likely im-

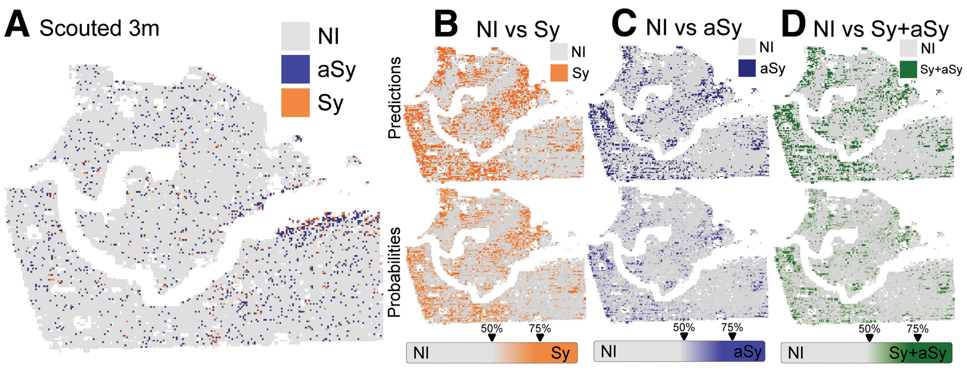

Fig. 5. A classified Airborne Visible and Infrared Imaging Spectrometer Next Generation spectroscopic image of a vineyard in Lodi, California, based on the random forest model SG-PCA-SMOTE at 3-m resampling resolution. Noninfected (NI), symptomatic (Sy), and asymptomatic vines (aSy). **A,** Scouted locations of grapevine leafroll-associated virus complex 3 are indicated at 3-m resolution. **B,** Predictions of a model trained to differentiate between NI and Sy + aSy showing the probability heat map. **C,** Predictions of a model trained to differentiate between NI and Sy showing the probability heat map. **D,** Predictions of a model trained to differentiate between NI and aSy showing the probability heat map.

pact model performance. Future work should investigate an expanded geographic range, such as different latitudes of California and different geographic regions, for example—the northeastern Great Lakes region, or areas in other wine-producing countries. Additionally, crop varieties are known to interact with pathogens differently (Gold et al. 2020b). In grapevines, for example, white grape varieties (e.g., Chardonnay) exhibit subtle to no foliar symptoms when infected with GLRaV-3, and some hybrids are known to have higher viral load tolerance that affects biological response (Naidu et al. 2014). In grape production, varieties are managed differently according to their individual requirements as well as the ultimate product (e.g., wine, juice, table, or raisin) for the grapes. These differences all influence spectral signals. Scientists aiming to use imaging spectroscopy for disease detection not only in grapevines, but any in cropping system, must take into consideration generalizability among varieties, geography, and management practices and quantify how each affects disease detection.

Interest in using nondestructive imaging spectroscopy to detect plant–microbe interactions has increased exponentially in recent years; however, most studies have focused on bacterial and fungal disease detection in tree crops (Sapes et al. 2022; Sousa et al. 2021; Zarco-Tejada et al. 2018). This study expands our current understanding of plant disease sensing by reporting for the first time the capacity for airborne imaging spectroscopy to detect plant–viral interactions in a nontree crop at multiple resolutions both pre- and postsymptomatically. The findings suggest that viral infection, regardless of visible symptom appearance, imparts a consistent, systemic change to foliar reflectance that can be detected with airborne imaging spectroscopy, and that this ability is improved by de-noising and dimensionality reduction techniques. A scalable, nondestructive, and low-cost solution for latent viral infection detection is a game-changing prospect for the grape industry and agriculture in general. Destructive molecular or serological testing remains the most accurate method of detecting viral infection at the asymptomatic stage; however, these methods cannot be scaled because of expense. The imaging spectroscopy described in this study is an initial step toward accurate and scalable early detection of grapevine viral infection that could be used to deploy ground mitigation efforts more strategically, such as scouting, molecular testing, and vine removal.

In conclusion, we find that airborne imaging spectroscopy and machine learning can be used to develop models that effectively identify the spectroscopic signal of GLRaV-3 infection in grapevines across various spatial resolutions, regardless of visible symptom manifestation. The goal of our work is not to replace existing field scouting strategies or molecular testing, but instead to deploy these resources more strategically to improve the overall financial, environmental, and societal sustainability of grape production. As we advance toward launch of NASA's Surface Biology and Geology study, a deployment of polar sun-synchronous satellites with hyperspectral and thermal capabilities (Stavros et al. 2023), it will be important to assess the scalability of our findings to the study's anticipated native resolution (~30 m), as well as to develop a user-friendly application for the grape and broader agricultural community to access the surface biology and geology data that requires minimal programming, remote sensing, or GIS expertise for use.

Acknowledgments

We thank Michael Eastwood and the many members of the NASA JPL AVIRIS-NG team who, along with Woody Turner, were responsible for initiating the successful air campaign that led to this publication; our industry collaborators for their invaluable efforts and collaboration in supporting this project; and the talented and hardworking scouting teams who spent countless hours in vineyards identifying and geotagging diseased vines to provide us with high-quality validation data.

Literature Cited

Agrios, G. N. 2009. Plant pathogens and disease: General introduction. Pages 613-646 in: Encyclopedia of Microbiology. Elsevier. Available at: https://linkinghub.elsevier.com/retrieve/pii/B9780123739445003448

Almeida, R. P. P., Daane, K. M., Bell, V. A., Blaisdell, G. K., Cooper, M. L., Herrbach, E., and Pietersen, G. 2013. Ecology and management of grapevine leafroll disease. Front. Microbiol. 4:94.

Arnold, K., Golino, D. A., and McRoberts, N. 2017. A synoptic analysis of the temporal and spatial aspects of grapevine leafroll disease in a historic Napa vineyard and experimental vine blocks. Phytopathology 107:418-426.

Bendel, N., Kicherer, A., Backhaus, A., Köckerling, J., Maixner, M., Bleser, E., Klück, H.-C., Seiffert, U., Voegele, R. T., and Töpfer, R. 2020. Detection of grapevine leafroll-associated virus 1 and 3 in white and red grapevine cultivars using hyperspectral imaging. Remote Sens. 12:1693.

Blaisdell, G. K., Cooper, M. L., Kuhn, E. J., Taylor, K. A., Daane, K. M., and Almeida, R. P. P. 2016. Disease progression of vector-mediated Grapevine leafroll-associated virus 3 infection of mature plants under commercial vineyard conditions. Eur. J. Plant Pathol. 146:105-116.

Bolton, S. 2020. What every winegrower should know: Viruses. Lodi Winegrape Commission, Lodi, CA.

Cabaleiro, C., and Segura, A. 2006. Temporal analysis of grapevine leafroll associated virus 3 epidemics. Eur. J. Plant Pathol. 114:441-446.

Calderón, R., Navas-Cortés, J. A., Lucena, C., and Zarco-Tejada, P. J. 2013. High-resolution airborne hyperspectral and thermal imagery for early detection of Verticillium wilt of olive using fluorescence, temperature and narrow-band spectral indices. Remote Sens. Environ. 139:231-245.

Chapman, J. W., Thompson, D. R., Helmlinger, M. C., Bue, B. D., Green, R. O., Eastwood, M. L., Geier, S., Olson-Duvall, W., and Lundeen, S. R. 2019. Spectral and radiometric calibration of the Next Generation Airborne Visible Infrared Spectrometer (AVIRIS-NG). Remote Sens. 11:2129.

Charles, J. G., Cohen, D., Walker, J. T. S., Forgie, S. A., Bell, V. A., and Breen, K. C. 2006. A review of the ecology of grapevine leafroll associated virus type 3 (GLRaV3). N.Z. Plant Prot. 59:330-337.

Charles, J. G., Froud, K. J., van den Brink, R., and Allan, D. J. 2009. Mealybugs and the spread of grapevine leafroll-associated virus 3 (GLRaV-3) in a New Zealand vineyard. Austral. Plant Pathol. 38:576.

Chlus, A., Winstonolson, Greenberg, E., and Oldmanye007. 2023. EnSpec/hytools: 1.5.0. https://zenodo.org/record/5997755

Couture, J. J., Singh, A., Rubert-Nason, K. F., Serbin, S. P., Lindroth, R. L., and Townsend, P. A. 2016. Spectroscopic determination of ecologically relevant plant secondary metabolites. Methods Ecol. Evol. 7:1402-1412.

Curran, P. J. 1989. Remote sensing of foliar chemistry. Remote Sens. Environ. 30:271-278.

Gao, B. 1996. NDWI—A normalized difference water index for remote sensing of vegetation liquid water from space. Remote Sens. Environ. 58:257-266.

Gao, Z., Khot, L. R., Naidu, R. A., and Zhang, Q. 2020. Early detection of grapevine leafroll disease in a red-berried wine grape cultivar using hyperspectral imaging. Comput. Electron. Agric. 179:105807.

Gillies, S., Ward, B., and Petersen, A. S. 2013. Rasterio: Geospatial raster I/O for Python programmers. https://github.com/mapbox/rasterio

Gold, K. M., Townsend, P. A., Chlus, A., Herrmann, I., Couture, J. J., Larson, E. R., and Gevens, A. J. 2020a. Hyperspectral measurements enable presymptomatic detection and differentiation of contrasting physiological effects of late blight and early blight in potato. Remote Sens. 12:286.

Gold, K. M., Townsend, P. A., Herrmann, I., and Gevens, A. J. 2020b. Investigating potato late blight physiological differences across potato cultivars with spectroscopy and machine learning. Plant Sci. 295:110316.

Habili, N., and Nutter, F. W. 1997. Temporal and spatial analysis of grapevine leafroll-associated virus 3 in pinot noir grapevines in Australia. Plant Dis. 81:625-628.

Hornero, A., Zarco-Tejada, P. J., Quero, J. L., North, P. R. J., Ruiz-Gómez, F. J., Sánchez-Cuesta, R., and Hernandez-Clemente, R. 2021. Modelling hyperspectral- and thermal-based plant traits for the early detection of *Phytophthora*-induced symptoms in oak decline. Remote Sens. Environ. 263:112570.

Jackson, R. D. 1986. Remote sensing of biotic and abiotic plant stress. Annu. Rev. Phytopathol. 24:265-287.

Kokaly, R., Clark, R. N., Swayze, G. A., Livo, K. E., Hoefen, T. M., Pearson, N. C., Wise, R. A., Benzel, W. M., Lowers, H. A., Driscoll, R. L., and Klein, A. J. 2017. USGS Spectral Library Version 7 Data. https://www.sciencebase.gov/catalog/item/5807a2a2e4b0841e59e3a18d

Lemaître, G., Nogueira, F., and Aridas, C. K. 2017. Imbalanced-learn: A Python Toolbox to tackle the curse of imbalanced datasets in machine learning. J. Mach. Learn. Res. 18:559-563.

López-López, M., Calderón, R., González-Dugo, V., Zarco-Tejada, P., and Fereres, E. 2016. Early detection and quantification of almond red leaf blotch using high-resolution hyperspectral and thermal imagery. Remote Sens. 8:276.

MacDonald, S. L., Staid, M., Staid, M., and Cooper, M. L. 2016. Remote hyperspectral imaging of grapevine leafroll-associated virus 3 in Cabernet Sauvignon vineyards. Comput. Electron. Agric. 130:109-117.

Maree, H. J., Almeida, R. P. P., Bester, R., Chooi, K. M., Cohen, D., Dolja, V. V., Fuchs, M. F., Golino, D. A., Jooste, A. E., Martelli, G. P., Naidu, R. A., Rowhani, A., Saldarelli, P., and Burger, J. T. 2013. Grapevine leafroll-associated virus 3. Front. Microbiol. 4:82.

Martin, R., Chadwick, K., Brodrick, P., Carranza-Jimenez, L., Vaughn, N., and Asner, G. 2018. An approach for foliar trait retrieval from airborne imaging spectroscopy of tropical forests. Remote Sens. 10:199.

Maxwell, A. E., Warner, T. A., and Fang, F. 2018. Implementation of machine-learning classification in remote sensing: An applied review. Int. J. Remote Sens. 39:2784-2817.

Meza Ramirez, C. A., Greenop, M., Ashton, L., and Rehman, I. 2021. Applications of machine learning in spectroscopy. Appl. Spectrosc. Rev. 56:733-763.

Nagarajan, S. 1984. Monitoring wheat rust epidemics with the Landsat-2 satellite. Phytopathology 74:585.

Naidu, R. A., Maree, H. J., and Burger, J. T. 2015. Grapevine leafroll disease and associated viruses: a unique pathosystem. Annu. Rev. Phytopathol. 53: 613-634.

Naidu, R. A., Perry, E. M., Pierce, F. J., and Mekuria, T. 2009. The potential of spectral reflectance technique for the detection of *Grapevine leafroll-associated virus-3* in two red-berried wine grape cultivars. Comput. Electron. Agric. 66:38-45.

Naidu, R., Rowhani, A., Fuchs, M., Golino, D., and Martelli, G. P. 2014. Grapevine leafroll: A complex viral disease affecting a high-value fruit crop. Plant Dis. 98:1172-1185.

Olmos, A., Bertolini, E., Ruiz-García, A. B., Martínez, C., Peiró, R., and Vidal, E. 2016. Modeling the accuracy of three detection methods of *Grapevine leafroll-associated virus 3* during the dormant period using a Bayesian approach. Phytopathology 106:510-518.

Oren, R., Schulze, E.-D., Matyssek, R., and Zimmermann, R. 1986. Estimating photosynthetic rate and annual carbon gain in conifers from specific leaf weight and leaf biomass. Oecologia 70:187-193.

Pedregosa, F., Varoquaux, G., Gramfort, A., Michel, V., Thirion, B., Grisel, O., Blondel, M., Prettenhofer, P., Weiss, R., Dubourg, V., Vanderplas, J., Passos, A., Cournapeau, D., Brucher, M., Perrot, M., and Duchesnay, E. 2011. Scikit-Learn: Machine learning in Python. J. Mach. Learn. Res. 12: 2825-2830.

Pietersen, G., Spreeth, N., Oosthuizen, T., van Rensburg, A., van Rensburg, M., Lottering, D., Rossouw, N., and Tooth, D. 2013. Control of grapevine leafroll disease spread at a commercial wine estate in South Africa: A case study. Am. J. Enol. Viticulture 64:296-305.

Queally, N., Ye, Z., Zheng, T., Chlus, A., Schneider, F., Pavlick, R. P., and Townsend, P. A. 2022. FlexBRDF: A flexible BRDF correction for grouped processing of airborne imaging spectroscopy flightlines. JGR Biogeosci. 127:e2021JG006622.

Sapes, G., Lapadat, C., Schweiger, A. K., Juzwik, J., Montgomery, R., Gholizadeh, H., Townsend, P. A., Gamon, J. A., and Cavender-Bares, J. 2022. Canopy spectral reflectance detects oak wilt at the landscape scale using phylogenetic discrimination. Remote Sens. Environ. 273: 112961.

Scheffler, D., Hollstein, A., Diedrich, H., Segl, K., and Hostert, P. 2017. AROSICS: An automated and robust open-source image co-registration software for multi-sensor satellite data. Remote Sens. 9:676.

Schneider, F. D., Morsdorf, F., Schmid, B., Petchey, O. L., Hueni, A., Schimel, D. S., and Schaepman, M. E. 2017. Mapping functional diversity from remotely sensed morphological and physiological forest traits. Nat. Commun. 8:1441.

Serbin, S. P., Wu, J., Ely, K. S., Kruger, E. L., Townsend, P. A., Meng, R., Wolfe, B. T., Chlus, A., Wang, Z., and Rogers, A. 2019. From the Arctic to the tropics: Multibiome prediction of leaf mass per area using leaf reflectance. New Phytol. 224:1557-1568.

Singh, A., Serbin, S. P., McNeil, B. E., Kingdon, C. C., and Townsend, P. A. 2015. Imaging spectroscopy algorithms for mapping canopy foliar chemical and morphological traits and their uncertainties. Ecol. Appl. 25: 2180-2197.

Sinha, R., Khot, L. R., Rathnayake, A. P., Gao, Z., and Naidu, R. A. 2019. Visible-near infrared spectroradiometry-based detection of grapevine leafroll-associated virus 3 in a red-fruited wine grape cultivar. Comput. Electron. Agric. 162:165-173.

Song, Y., Hanner, R. H., and Meng, B. 2021. Probing into the effects of grapevine leafroll-associated viruses on the physiology, fruit quality and gene expression of grapes. Viruses 13:593.

Sousa, D., Brodrick, P., Cawse-Nicholson, K., Fisher, J. B., Pavlick, R., Small, C., and Thompson, D. R. 2022. The spectral mixture residual: A source of low-variance information to enhance the explainability and accuracy of surface biology and geology retrievals. JGR Biogeosci. 127:e2021JG006672.

Sousa, D., Fisher, J. B., Galvan, F. R., Pavlick, R. P., Cordell, S., Giambelluca, T. W., Giardina, C. P., Gilbert, G. S., Imran-Narahari, F., Litton, C. M., Lutz, J. A., North, M. P., Orwig, D. A., Ostertag, R., Sack, L., and Phillips, R. P. 2021. Tree canopies reflect mycorrhizal composition. Geophys. Res. Lett. 48:e2021GL092764.

Stavros, E. N., Chrone, J., Cawse-Nicholson, K., Freeman, A., Glenn, N. F., Guild, L., Kokaly, R., Lee, C., Luvall, J., Pavlick, R., Poulter, B., Schollaert Uz, S., Serbin, S., Thompson, D. R., Townsend, P. A., Turpie, K., Yuen, K., Thome, K., Wang, W., Zareh, S.-K., Nastal, J., Bearden, D., Miller, C. E., and Schimel, D. 2023. Designing an observing system to study the surface biology and geology (SBG) of the Earth in the 2020s. JGR Biogeosci. 128:e2021JG006471.

Sun, Y., Frankenberg, C., Wood, J. D., Schimel, D. S., Jung, M., Guanter, L., Drewry, D. T., Verma, M., Porcar-Castell, A., Griffis, T. J., Gu, L., Magney, T. S., Köhler, P., Evans, B., and Yuen, K. 2017. OCO-2 advances photosynthesis observation from space via solar-induced chlorophyll fluorescence. Science 358:eaam5747.

Thompson, D. R., Natraj, V., Green, R. O., Helmlinger, M. C., Gao, B.-C., and Eastwood, M. L. 2018. Optimal estimation for imaging spectrometer atmospheric correction. Remote Sens. Environ. 216:355-373.

Tsai, F., and Philpot, W. 1998. Derivative analysis of hyperspectral data. Remote Sens. Environ. 66:41-51.

Virtanen, P., Gommers, R., Oliphant, T. E., Haberland, M., Reddy, T., Cournapeau, D., Burovski, E., Peterson, P., Weckesser, W., Bright, J., van der Walt, S. J., Brett, M., Wilson, J., Millman, K. J., Mayorov, N., Nelson, A. R. J., Jones, E., Kern, R., Larson, E., Carey, C. J., Polat, I., Feng, Y. u, Moore, E. W., VanderPlas, J., Laxalde, D., Perktold, J., Cimrman, R., Henriksen, I., Quintero, E. A., Harris, C. R., Archibald, A. M., Ribeiro, A. H., Pedregosa, F., van Mulbregt, P., Vijaykumar, A., Bardelli, A. P., Rothberg, A., Hilboll, A., Kloeckner, A., Scopatz, A., Lee, A., Rokem, A., Woods, C. N., Fulton, C., Masson, C., Häggström, C., Fitzgerald, C., Nicholson, D. A., Hagen, D. R., Pasechnik, D. V., Olivetti, E., Martin, E., Wieser, E., Silva, F., Lenders, F., Wilhelm, F., Young, G., Price, G. A., Ingold, G.-L., Allen, G. E., Lee, G. R., Audren, H., Probst, I., Dietrich, J. P., Silterra, J., Webber, J. T., Slavič, J., Nothman, J., Buchner, J., Kulick, J., Schönberger, J. L., de Miranda Cardoso, J. V., Reimer, J., Harrington, J., Rodríguez, J. L. C., Nunez-Iglesias, J., Kuczynski, J., Tritz, K., Thoma, M., Newville, M., Kümmerer, M., Bolingbroke, M., Tartre, M., Pak, M., Smith, N. J., Nowaczyk, N., Shebanov, N., Pavlyk, O., Brodtkorb, P. A., Lee, P., McGibbon, R. T., Feldbauer, R., Lewis, S., Tygier, S., Sievert, S., Vigna, S., Peterson, S., More, S., Pudlik, T., Oshima, T., Pingel, T. J., Robitaille, T. P., Spura, T., Jones, T. R., Cera, T., Leslie, T., Zito, T., Krauss, T., Upadhyay, U., Halchenko, Y. O., and Vázquez-Baeza, Y. 2020. SciPy 1.0: Fundamental algorithms for scientific computing in Python. Nat. Methods 17: 261-272.

Zarco-Tejada, P. J., Camino, C., Beck, P. S. A., Calderon, R., Hornero, A., Hernández-Clemente, R., Kattenborn, T., Montes-Borrego, M., Susca, L., Morelli, M., Gonzalez-Dugo, V., North, P. R. J., Landa, B. B., Boscia, D., Saponari, M., and Navas-Cortes, J. A. 2018. Previsual symptoms of *Xylella fastidiosa* infection revealed in spectral plant-trait alterations. Nat. Plants 4:432-439.

Zarco-Tejada, P. J., Poblete, T., Camino, C., Gonzalez-Dugo, V., Calderon, R., Hornero, A., Hernandez-Clemente, R., Román-Écija, M., Velasco-Amo, M. P., Landa, B. B., Beck, P. S. A., Saponari, M., Boscia, D., and Navas-Cortes, J. A. 2021. Divergent abiotic spectral pathways unravel pathogen stress signals across species. Nat. Commun. 12:6088.

Zhu, X., Li, X., Jiu, S., Zhang, K., Wang, C., and Fang, J. 2018. Analysis of the regulation networks in grapevine reveals response to waterlogging stress and candidate gene-marker selection for damage severity. R. Soc. Open Sci. 5:172253.